Acta Mech 205, 171–183 (2009)
DOI 10.1007/s00707-009-0172-5

Andrés A. Peña · Pedro G. Lind · Sean McNamara · Hans J. Herrmann

Geometrical derivation of frictional forces for granular media under slow shearing

Received: 23 September 2007 / Revised: 5 May 2008 / Published online: 4 April 2009

Abstract We present an alternative way to determine the frictional forces at the contact between two particles. This alternative approach has its motivation in a detailed analysis of the bounds on the time integration step in the discrete element method for simulating collisions and shearing of granular assemblies. We show that, in standard numerical schemes, the upper limit for the time integration step, usually taken from the average time t_c of one contact, is in fact not sufficiently small to guarantee numerical convergence of the system during relaxation. In particular, we study in detail how the kinetic energy decays during the relaxation stage and compute the correct upper limits for the time integration step, which are significantly smaller than the ones commonly used. In addition, we introduce an alternative approach based on simple relations to compute the frictional forces that converges even for time integration steps above the upper limit.

1 Introduction

One of the standard approaches to model the dynamics of granular media is to use the discrete element method (DEM) [1–3], e.g., to study shear [4–8]. Some problems may arise due to the need to use large time integration steps to perform numerical simulations with reasonable computational effort without compromising the overall convergence of the numerical scheme chosen.

An efficient method for the numerical integration of systems of coupled differential equations, particularly suited for granular media [1] is the so-called Gear algorithm. One important feature of the Gear algorithm is its numerical stability, making it particularly suited for granular particle systems where short range interactions co-exist with strong gradients. This algorithm consists of two main steps, one where particle positions and higher-order derivatives are predicted and another where they are corrected. A short description of this

A. A. Peña · P. G. Lind · S. McNamara
Institute for Computational Physics, Universität Stuttgart, Pfaffenwaldring 27, 70569 Stuttgart, Germany

A. A. Peña
Bilfinger Berger GmbH, Civil, Structural Design, 65189 Wiesbaden, Germany

P. G. Lind
Centro de Física Teórica e Computacional, Av. Prof. Gama Pinto 2, 1649-003 Lisbon, Portugal

H. J. Herrmann
Departamento de Física, Universidade Federal do Ceará, Fortaleza, Ceará 60451-970, Brazil

H. J. Herrmann (✉)
Computational Physics, IfB, HIF E12, ETH Hönggerberg, 8093 Zurich, Switzerland
E-mail: hans@ifb.baug.ethz.ch

algorithm is given in the Appendix. Usually, one assumes an upper limit for the admissible integration steps based on empirical reasoning [9].

While such numerical schemes chosen to integrate the equations of motion are of importance, it is known [1] that a substantial part of the computation efforts is spent on the evaluation of the forces acting on each particle at each time step. For that reason, as we will see, the time integration step used for the computation of the forces is sometimes larger than the one of the integration scheme for the equations of motion. While such a difference is not critical in some shear systems, for slow shearing it plays a non-negligible role.

For slow shearing, the convergence of numerical schemes is particularly important when studying for instance the occurrence of avalanches [8] and the emergence of ratcheting in cyclic loading [10].

In this paper we show that the time integration step able to guarantee convergence of the numerical scheme, must in general be smaller than a specific upper limit, significantly below the commonly accepted value [5,9,11]. This upper limit strongly depends on (i) the accuracy of the approach used to calculate frictional forces between particles, (ii) on the corresponding duration of the contact and (iii) on the number of degrees of freedom. To illustrate this fact, we address the specific case of slow shearing, for which the above limit is too small to allow for reasonable computation time. Here, we concentrate on the accuracy of the total kinetic energy of the system in a stress-controlled test. The total kinetic energy is one of the important quantities in several systems under slow shearing, such as tectonic systems, for which the study and forecasting of avalanches and earthquakes rely significantly on the accurate computation of the kinetic energy released by the system.

Additionally, we show that the need of a small time integration step is related to the scheme used to compute the frictional forces, namely the Cundall spring model. To overcome the shortcoming present in the Cundall spring model, we propose an alternative approach that corrects the frictional contact forces, when large time integration steps are taken. In this way, we enable the use of considerably larger integration steps, assuring at the same time the convergence of the integration scheme used for the equations of motion.

We start in Sect. 2 by presenting in some detail the DEM [1,9,12]. Sections 3 and 4 describe, respectively, the dependence on the time integration step and the improved algorithm. Discussions and conclusions are given in Sect. 5.

2 The model

We consider a two-dimensional system of polygonal particles, each one having two linear and one rotational degree of freedom. The evolution of the system is given by Newton's equations of motion, where the resulting forces and moments acting on each particle i are given by the sum of all forces and moments applied on that particle:

$$m_i \ddot{\boldsymbol{r}}_i = \sum_c \boldsymbol{F}_i^c + \sum_{c_b} \boldsymbol{F}_i^b, \tag{1a}$$

$$I_i \ddot{\boldsymbol{\theta}}_i = \sum_c \boldsymbol{l}_i^c \times \boldsymbol{F}_i^c + \sum_{c_b} \boldsymbol{l}_i^b \times \boldsymbol{F}_i^b, \tag{1b}$$

where m_i denotes the mass of particle i, I_i its moment of inertia, and $\boldsymbol{l}$ the branch vector which connects the center of mass of the particle to the application point of the contact force $\boldsymbol{F}_i^c$ or boundary force $\boldsymbol{F}_i^b$. The sum in c is over all the particles in contact with polygon i, and the sum in c_b is over all the vertices of polygon i in contact with the boundary. One integrates Eq. (1) for all particles $i = 1, \ldots, N$ and obtains the evolution of their centers of mass $\boldsymbol{r}_i$ and rotation angles θ_i.

Further, during loading, particles tend to deform each other. This deformation of the particles is usually reproduced by letting them overlap [1,12], as illustrated in Fig. 1. The overlap between each pair of particles is considered to fully characterize the contact. Namely, the normal contact force is assumed to be proportional to the overlap area [13] and its direction perpendicular to the plane of contact, which is defined by the intersection between the boundaries of the two particles.

All the dynamics is deduced from the contact forces acting on the particles. The contact forces, $\boldsymbol{F}^c$, either between particles or with the boundary, are decomposed into their elastic and viscous contributions, $\boldsymbol{F}^e$ and $\boldsymbol{F}^v$, respectively, yielding $\boldsymbol{F}^c = \boldsymbol{F}^e + \boldsymbol{F}^v$.

The viscous force is important for maintaining the numerical stability of the method and to take into account dissipation at the contact. This force is calculated as [12]

$$\boldsymbol{F}^v = -m_r \nu \boldsymbol{v}^c, \tag{2}$$

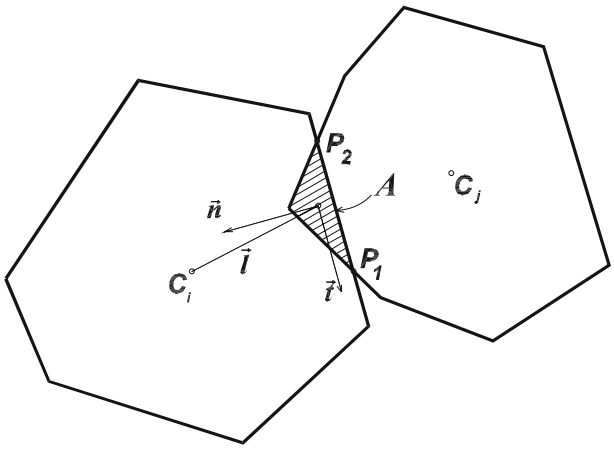

Fig. 1 Illustration of two overlapping particles. The overlap region A between particles fully characterizes the contact force $\boldsymbol{F}^c$ (see text)

where $m_r = (1/m_i + 1/m_j)^{-1}$ is the reduced mass of the two particles, i and j, and ν is the damping coefficient. The relative velocity at the contact point is defined as

$$\boldsymbol{v}^c = \boldsymbol{v}_i - \boldsymbol{v}_j + \boldsymbol{w}_i \times \boldsymbol{l}_i - \boldsymbol{w}_j \times \boldsymbol{l}_j \tag{3}$$

at the contact point. Here, $\boldsymbol{v}_i$ and $\boldsymbol{v}_j$ are the linear velocities of the centers of mass and $\boldsymbol{w}_i$ and $\boldsymbol{w}_j$ the angular velocities of the particles around the corresponding centers of mass.

The elastic part of the contact force is what will be carefully studied, since it is what determines the accuracy of the integration scheme. The term $\boldsymbol{F}^e$ is simply given by the sum of the normal and the tangential components, with respect to the contact plane, namely

$$\boldsymbol{F}^e = F_n^e \hat{n}^c + F_t^e \hat{t}^c, \tag{4}$$

where the normal component reads

$$F_n^e = -k_n A / l_c, \tag{5}$$

with k_n the normal stiffness, A the overlap area and $l_c = r_i + r_j$ the characteristic length of the contact between particles i and j, with $r_i = \sqrt{A_i/\pi}$ and A_i the area of the particle i (and similarly for particle j).

Using an extension of the Cundall–Stack spring [12], which considers the tangential force to be proportional to the elastic elongation ξ of an imaginary spring at the contact, one defines the static frictional force between each pair of particles in contact, as

$$F_t^e = -k_t \xi, \tag{6}$$

where k_t is the tangential stiffness. This tangential force assumes each contact as being described by a damped oscillator with some frequency ω (see below).

The elastic elongation ξ in Eq. (6) is updated as

$$\xi(t + \Delta t) = \xi(t) + \boldsymbol{v}_t^c \Delta t, \tag{7}$$

where Δt is the time step of the DEM simulation, and $\boldsymbol{v}_t^c$ is the tangential component of the relative velocity $\boldsymbol{v}^c$ at the contact point. The tangential elastic elongation ξ changes according to Eq. (7) whenever the condition $|F_e^t| < \mu F_e^n$ is satisfied; whereas, when the Coulomb limit condition $|F_e^t| = \mu F_e^n$ is reached, sliding is enforced by keeping the tangential force F_e^t constant and assigning to ξ its extreme values $\pm \mu k_n A/(k_t l_c)$. This latter Coulomb condition corresponds to the regime where particles behave inelastically, while the former inequality describes the forces when the particles behave elastically. Parameter μ is the inter-particle friction coefficient.

Since the accuracy of elongation ξ directly affects the calculation of the tangential force in Eq. (6), macroscopic quantities of interest, such as the shear resistance, are also affected by the time step Δt chosen for Eq. (7).

As said above, in DEM, one of the numerical integration schemes usually used to solve the equations of motion above is the Gear's predictor–corrector scheme [9]. This scheme consist of three main stages, namely prediction, evaluation, and correction (see the Appendix for details). Using this numerical scheme we integrate equations of the form $\ddot{\boldsymbol{r}} = f(\boldsymbol{r}, \dot{\boldsymbol{r}})$, using a fifth order predictor–corrector algorithm that has a numerical error proportional to $(\Delta t)^6$ for each time integration step [9]. However, as will be seen in Sect. 3, $(\Delta t)^6$ is not the numerical error of the full integration scheme, since Eq. (6), used to calculate the frictional force, is of order $(\Delta t)^2$.

For a certain value of normal contact stiffness k_n, almost any value for the normal damping coefficient ν_n might be selected. Their relation defines the restitution coefficient ϵ obtained experimentally for various materials [14]. The restitution coefficient is given by the ratio between the relative velocities after and before a collision. In particular, the normal restitution coefficient ϵ_n can be written as a function of k_n and ν_n [15], namely

$$\epsilon_n = \exp\left(-\pi\eta/\omega\right) = \exp\left(-\frac{\pi}{\sqrt{4m_r k_n/\nu_n^2 - 1}}\right), \tag{8}$$

where $\omega = \sqrt{\omega_0^2 - \eta^2}$ is the frequency of the damped oscillator, with $\omega_0 = \sqrt{k_n/m_r}$ the frequency of the elastic oscillator, m_r the reduced mass and $\eta = \nu_n/(2m_r)$ the effective viscosity. The tangential component ϵ_t of the restitution coefficient is defined similarly using k_t and ν_t in Eq. (8).

Therefore, a suitable closed set of parameters for this model are the ratios k_t/k_n and ϵ_t/ϵ_n, ν_t/ν_n, together with the normal stiffness k_n and the interparticle friction μ. For simplicity we will always take $\nu_t/\nu_n = k_t/k_n$ which is assumed to be constant, as done in previous studies [6].

The entire algorithm above relies on a proper choice of the integration step Δt, which should neither be too large to avoid divergence of the integration nor too small avoiding unreasonably long computational time. The determination of the optimal time integration step varies from case to case and one usually assumes the possible main criteria to estimate an upper bound for admissible time integration steps.

The first criterion is to use the characteristic period of oscillation [9], defined as

$$t_s = 2\pi\sqrt{\frac{\langle m\rangle}{k_n}}, \tag{9}$$

where $\langle m\rangle$ is the smallest particle mass in the system. For a fifth order predictor–corrector integration scheme, it is usually accepted that a safe time integration step should be below a threshold of $\Delta t < t_s/10$ [9].

The second criterion is to extract the threshold from local contact events [5,11,15], namely from the characteristic duration of a contact:

$$t_c = \frac{\pi}{\sqrt{\omega_0^2 - \eta^2}}. \tag{10}$$

Both criteria can be assumed to be equivalent, since typically $t_c \simeq t_s/2$, and therefore in such cases, one considers as an admissible time integration steps such that $\Delta t < t_c/5$ [15,16].

In the next section we will study in detail the integration for different values of the model parameters.

3 The choice of the time integration step

We simulate the relative motion of two plates shearing against each other [7,8,13]. Considering a system of 256 particles as illustrated in Fig. 2, where both top and bottom boundaries move in opposite directions with a constant shear rate $\dot{\gamma}$. The top and bottom layer of the sample have fixed boundary conditions, while horizontally we consider periodic boundary conditions. The volumetric strain is suppressed, i.e., the vertical position of the walls is fixed and there is no dilation. The particles of the fixed boundary are not allowed to rotate or move against each other. The shear rate is $\dot{\gamma} = 1.25\times10^{-5}\mathrm{s}^{-1}$, the parameter values are $k_n = 400$ N/m, $\epsilon_n = 0.9875$, and $\mu = 0.5$. The relation k_t/k_n is chosen such that $k_t < k_n$, similar to previous studies [12,15,17], namely $k_t/k_n = \nu_t/\nu_n = 1/3$, which when substituted in Eq. (8) yields $\epsilon_t/\epsilon_n = 1.0053$.

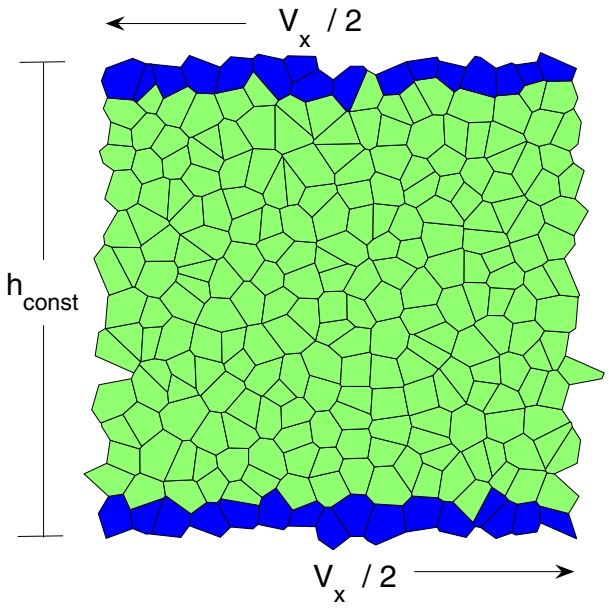

Fig. 2 Sketch of the system of 256 particles (*light particles*, *green in color*) under shearing of top and bottom boundaries (*dark particles*, *blue in color*). Horizontally periodic boundary conditions are considered and a constant low shear rate is chosen (see text)

By integrating such a system of particles using the scheme described in the previous section, one can easily compute the kinetic energy E_k of a given particle i,

$$E_k(i) = \frac{1}{2}\left(m_i \dot{\boldsymbol{r}}_i^2 + I_i \boldsymbol{\omega}_i^2\right), \tag{11}$$

where the velocity $\dot{\boldsymbol{r}}$ is computed from the predictor–corrector algorithm, I_i is the moment of inertia of the polygon and $\boldsymbol{\omega}_i$ is the angular velocity. The total kinetic energy of the full system of particles is given just by the sum of $E_k(i)$ over all the particles.

In Fig. 3, we show the evolution of the total kinetic energy for two different $\Delta t/t_c = 13/2{,}500 t_c$ and $13/500 t_c$. This kinetic energy is of the same order of magnitude as the corresponding elastic energy. As one sees, frictionless particles (Fig. 3a, c) have an E_k that does not change for different integration steps, while when $\mu = 0.5$ (Fig. 3b, d) the evolution of E_k strongly depends on Δt. In Fig. 3e we plot the cumulative difference ΔE_k between the values of E_k taken for each time integration step. Here, one sees that in the absence of friction ΔE_k is significantly lower then when friction is present.

From Fig. 3, one concludes that the expected upper limit $\sim t_c/5$, usually assumed and mentioned in the previous section, is still too large to guarantee convergence of the integration scheme when friction is considered.

To obtain a proper time integration step as function of the parameters of our model we next perform a careful analysis. If the commonly upper bound considered for the integration steps are valid in large systems, they must also be valid for single pairs of overlapping particles, even in the case when particles have a regular form, say discs. We will show that even in such small and simple systems lower bounds for the time integration step must be considered. In particular, at the usual bounds the kinetic energy of a stress-controlled test of two particles still does not decay at the proper rate.

As sketched in Fig. 4, we consider the simple situation of two circular particles and study the kinetic energy of one of them under external forcing, as sketched in Fig. 4. We start with two touching discs, i and j, where one of them, say i, remains fixed, while the other is subject to a force $\boldsymbol{F}$ perpendicular to its surface (no external torque is induced) along the x-axis. As a result of this external force, the disc j undergoes rotation. The contact force is obtained from the corresponding springs that are computed, as described in Sect. 2, and acts against the external force. This results in an oscillation of disc j till relaxation (dashed circle in Fig. 4) with a final center of mass displacement of ΔR and a rotation around the center of mass of $\Delta\theta$. Since $\boldsymbol{F}$ is kept constant, the procedure is stress controlled.

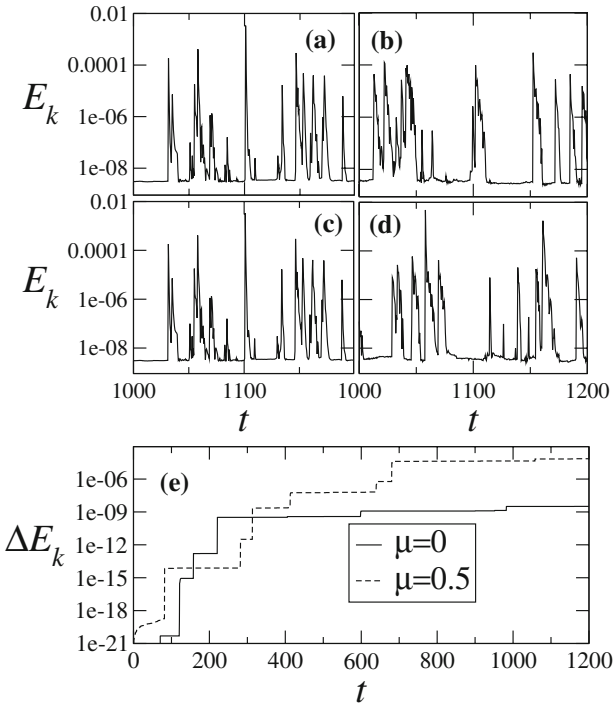

Fig. 3 Dependence of the Gear's numerical scheme on the time integration step Δt and the friction coefficient μ, by plotting the kinetic energy E_k as a function of time, for **a** $\Delta t/t_c = 13/2{,}500t_c$ and $\mu = 0$ (no friction), **b** $\Delta t/t_c = 13/2{,}500t_c$ and $\mu = 0.5$, **c** $\Delta t/t_c = 13/500t_c$ and $\mu = 0$, and **d** $\Delta t/t_c = 13/500t_c$ and $\mu = 0.5$. In **e** we show the difference between the values of E_k obtained with the two values of Δt. Here, $k_n = 400$ and the parametric relations in Eq. (9) and (10) are used (see text)

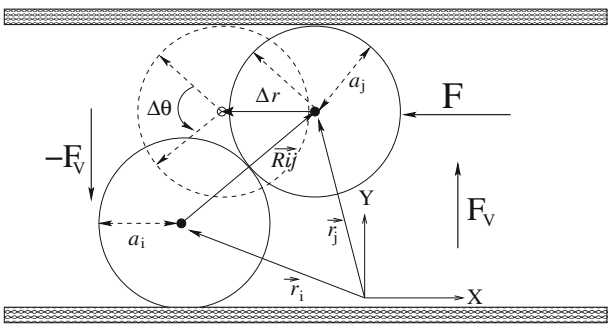

Fig. 4 Sketch of the stress-controlled test of two particles (*discs*). The particle located at $\boldsymbol{r}_i$ remains fixed, while the particle at $\boldsymbol{r}_j$ is initially touching particle i. The vector $\boldsymbol{R}_{ij}$ connecting the center of mass of particles i and j is initially oriented 45^o with respect to the x-axis. After applying the constant force $\boldsymbol{F}$ to disc j, the system relaxes to a new position (*dashed circumference*). Between its initial and final position particle j undergoes a displacement Δr and a rotation $\Delta\theta$ (see text). Forces F_V and $-F_V$ act on the upper and lower particle to balance the reaction from the wall. So the relaxation depends only on the force F

For the two discs sketched in Fig. 4, we plot in Fig. 5 the kinetic energy as a function of time, from the beginning until relaxation, using different integration steps, namely $\Delta t/t_c = 10^{-1}, 2\times10^{-2}, 10^{-2}, 10^{-3}$, and 10^{-4}. As we see, the kinetic energy decays exponentially,

$$E_k(t) = E_k^{(0)} \exp\left(-\frac{t}{t_R(\Delta t)}\right), \tag{12}$$

where t_R is a relaxation time whose value clearly depends on the time integration step Δt. As illustrated in the inset of Fig. 5, this change in t_R is not observed when friction is absent ($\mu = 0$), since no tangential forces are considered ($F_e^t = 0$).

Next, we will show that this dependence of t_R on Δt vanishes for

$$\Delta t \lesssim T_t(\mu)t_c, \tag{13}$$

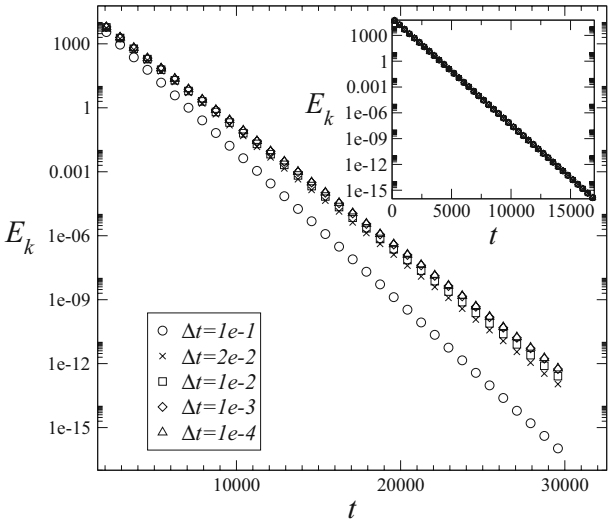

Fig. 5 The relaxation of the system of two discs sketched in Fig. 4. Here, we plot the kinetic energy E_k as a function of time t (in units of t_c) for different integration increments Δt and using a stiffness $k_n = 4 \times 10^8$ N/m and a friction coefficient $\mu = 500$. The large μ value is chosen so that the system remains in the elastic regime. As one sees, the relaxation time t_R converges to a constant value when Δt is sufficiently small (see text). This discrepancy between the values of t_R when different time integration steps are used does not occur in the absence of friction ($\mu = 0$), as illustrated in the inset. The slope of the *straight lines* is $-1/t_R$ (see Eq. 12)

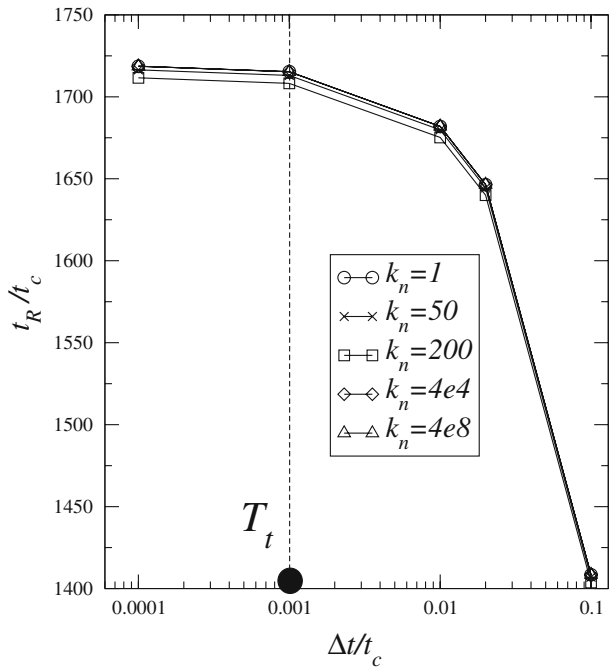

Fig. 6 The relaxation time t_R (in units of t_c) as a function of the normalized time integration step $\Delta t/t_c$, where the contact time t_c is defined in Eq. (10). Here, the friction coefficient is kept fixed $\mu = 500$ and different stiffnesses k_n (in units of N/m) are considered. The quotient $\Delta t/t_c$ collapses all the curves for different k_n. As a final result one finds a constant $T_t = 10^{-3}$ (*dashed vertical line*)

where $T_t(\mu)$ is a specific function that can only depend on μ, since from dimensional analysis it is clear that it is independent of k_n.

Figure 6 shows the relaxation time t_R of the kinetic energy of the two-particle system for different values of stiffnesses, namely for $k_n = 1, 50, 200 \times 10^4$ and 10^8 N/m. For all k_n values, one sees that, for decreasing Δt, the relaxation time t_R increases until it converges to a maximum. The stabilization of t_R occurs when Δt

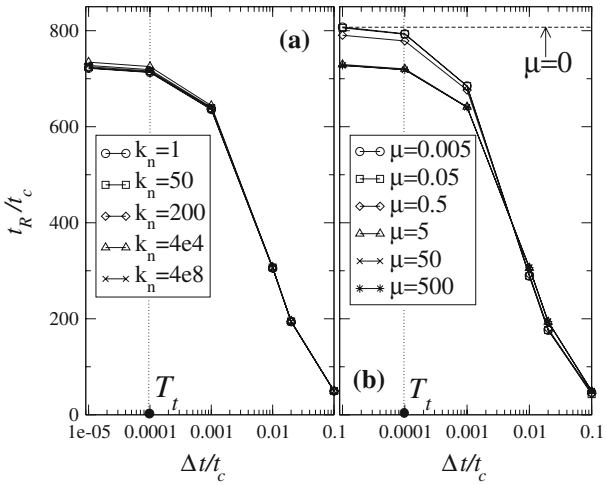

Fig. 7 The relaxation time t_R (in units of t_c) of the kinetic energy as a function of the normalized time integration step $\Delta t/t_c$, when rotation is suppressed. **a** $\mu = 500$ and different values of k_n and for **b** $k_n = 4 \times 10^8$ and different values of μ. The *dashed horizontal line* $\mu = 0$ in **b** indicates the relaxation time of the kinetic energy in the absence of friction (see text)

is small compared to the natural period $1/\omega_0$ of the system. We define T_t as the largest value of Δt for which we have this maximal relaxation time.

Further, all curves can be collapsed by using the normalized time integration step $\Delta t/t_c$. From Eq. (10) we calculate the contact times corresponding to these k_n values as $t_c = 1.969, 0.278, 0.139, 9.8 \times 10^{-2}$, and 9.8×10^{-5} s, respectively. Notice from Eq. (10) that the relaxation time scales with the stiffness as $t_c \sim k_n^{-1/2}$ (see Eq. 10).

From Fig. 6 one can conclude that the relaxation time converges when the time integration step obeys Eq. (13) with $T_t = 10^{-3}$ (dashed vertical line). In Fig. 6 both translation and rotation of particles are considered. The rotation of particles is usually of crucial interest, for instance to simulate rolling [7,18]. But suppressing rotation can also be of interest, for instance when simulating fault gouges: by hindering the rotation of particles, one can mimic young faults where a strong interlocking between the constituent rocks is expected [7].

To study this scenario, we present in Fig. 7a the relaxation time for the same parameter values as in Fig. 6, now disabling rotation. Here, we obtain a constant $T_t = 10^{-4}$ also, independent of k_n, one order of magnitude smaller than the previous value in Fig. 6. In other words, when rotation is suppressed, one must consider time integration steps typically one order of magnitude smaller than in the case when the discs are able to rotate. This can be explained as follows.

Though simulations do not require very small integration time steps when angular quantities are not taken into account, when suppressing rotation, one restricts the system to have a single degree of freedom. This restriction is done by enforcing at each time step a zero angular displacement in the predictor–corrector scheme for the particle under stress controlled test. Such a scenario is equivalent to the introduction of an additional force in the moving particle, preventing it to rotate. Thus, while this force induces faster relaxation, it varies during the simulation making the system more sensitive to the time integration step, i.e., yielding a smaller bound T_t. By comparing Fig. 7a with Fig. 6, one sees that the relaxation time t_R is smaller when rotation is suppressed.

From the bounds on the integration steps obtained above, one realizes that, in general, the correct time integration step must be significantly smaller than usually assumed.

While Fig. 7a clearly shows that t_R does not depend on the stiffness k_n, from Fig. 7b one sees that the same is not true for the friction coefficient μ. Indeed, from Fig. 8a one sees that there is a change of the relaxation time around $\mu = 1$. Here, the values correspond to a normalized time integration step $\Delta t/t_c = 10^{-5}$ for which t_R has already converged. This transition, which is not observed when rotation is considered (not shown), occurs since for larger values of $\mu > 1$, one has $F_t > F_n$, and therefore the frictional force increases and drives the system to relax faster. Further, with rotation one observes a larger t_R because there is an additional degree of freedom that also relaxes.

We also check the dependence of the relaxation time on the stiffness ratio k_t/k_n and on the restitution coefficient ratio ϵ_t/ϵ_n. For the stiffness ratio, we find that the convergence to a stationary value of t_R is faster

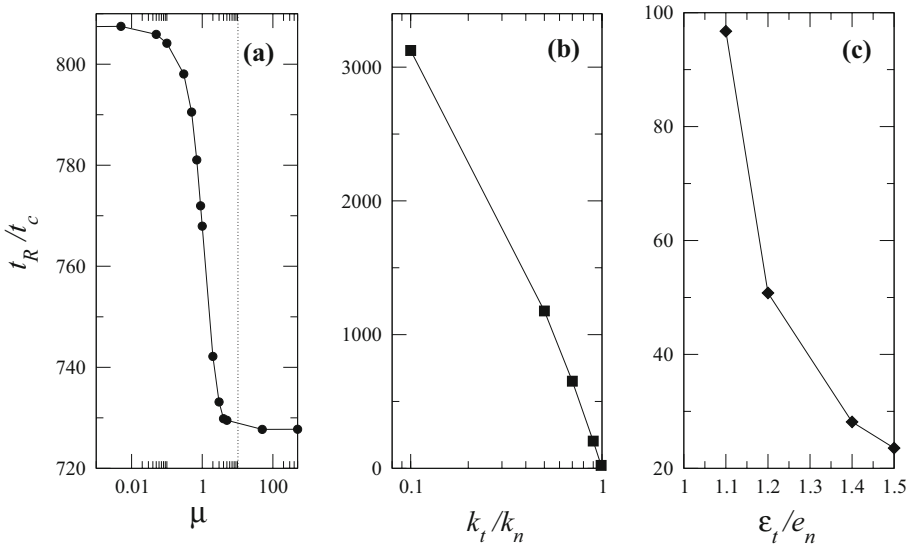

Fig. 8 The relaxation time t_R (in units of t_c) as a function **a** of the friction coefficient μ when rotation is suppressed, with $k_n = 4 \times 10^8$ N/m which corresponds to a contact time $t_c = 9.8 \times 10^{-5}$ s, **b** of the stiffness ratio k_t/k_n with $\mu = 500$ and $\epsilon_t/\epsilon_n = 1.0053$ and **c** of the restitution coefficients ratio ϵ_t/ϵ_n with $\mu = 500$ and $k_t/k_n = 1/3$. The normalized time integration step is $\Delta t/t_c = 10^{-5}$. *Dotted line* in **a** indicates the approximate maximum relevant value of μ in shearing systems

for large stiffness ratio as $k_t/k_n \to 1$, yielding larger values of T_t. Further, the stationary value of t_R logarithmically decreases with the stiffness ratios (see Fig. 8b), which can be explained from direct inspection of Eq. (8). Figure 8c, showing the relaxation time as a function of the ratio ϵ_t/ϵ_n for fixed $\mu = 500$ and $k_t/k_n = 1/3$, can be explained similarly as in Fig. 8b. Here, the dependence of the stationary value of t_R on ϵ_t/ϵ_n is approximately exponential.

All the correct relaxation times found above are obtained for the upper bound $T_t = 10^{-3}$. Further, we also notice that the results above were taken whenever the condition $|F_e^t| < \mu F_e^n$ is satisfied, since only in that case Eq. (7) is used (see Sect. 2). This fact indicates that the improvements in the algorithm should be implemented when computing the elastic component of the tangential contact force, in Eq. (7), as explained in the next section.

4 Improved approach to integrate the contact force

In this section we will describe a technique to overcome the need of very small time integration steps. As shown previously, when using Cundall's spring [4], the relaxation time of the two particles only converges when Δt is a small fraction T_t of the contact time t_c. This is due to the fact that the elastic elongation is assumed to be linear in Δt, i.e., the finite difference scheme in Eq. (7) is of very low order, $(\Delta t)^2$, compromising the convergence of the Gear's numerical scheme that is of order $(\Delta t)^6$. Therefore, the most plausible way to improve our algorithm is by choosing a different expression to compute the elastic tangential elongation ξ without using Eq. (7). Recently, it was reported [10] that the elastic potential energy stored in the contact is path-dependent. Consequently, an accurate computation of the frictional force would not be improved by an integration scheme—that is also path dependent—but, instead, we must assure that the computation of the frictional force does not depend on the time integration step.

We will introduce an expression for ξ that contains only the quantities computed in the predictor step. In this way we guarantee that ξ has errors of the order of $(\Delta t)^6$, instead of $(\Delta t)^2$, as it is the case of Eq. (7). Let us illustrate our approach on the simple system of two discs considered in the previous section (see Fig. 4).

On one side, if rotation is not allowed, the elastic elongation ξ depends only on the relative position of the two particles. In this case we substitute Eq. (7) by the expression

$$\xi_j^{(\mathrm{tr})}(t + \Delta t) = \xi_j^{(\mathrm{tr})}(t) + \frac{a_i}{a_i + a_j}(\boldsymbol{R}_{ij}^p(t + \Delta t) - \boldsymbol{R}_{ij}^p(t)) \times \hat{t}^c, \tag{14}$$

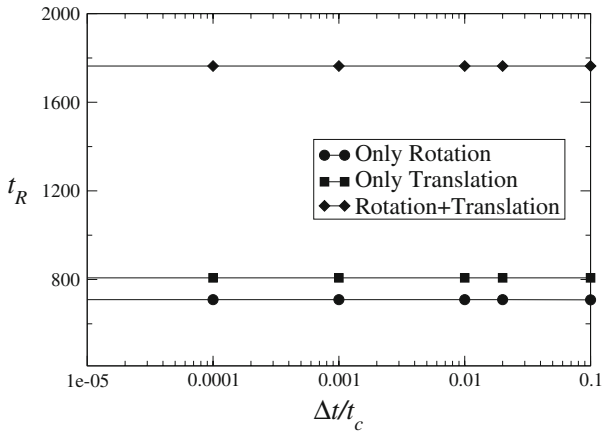

Fig. 9 The relaxation time t_R (in units of t_c) using Eqs. (14) and (15) between two discs, as illustrated in Fig. 4. For the three cases when considering only rotation, only translation or both, the relaxation time remains constant independent of the time integration step

where a_i and a_j are the radii of the discs i and j, respectively, $\boldsymbol{R}_{ij}$ is the vector joining both centers of mass and points in the direction $i \rightarrow j$ (see Fig. 4). The index p indicates quantities derived from the coordinates computed at the predictor step.

On the other side, if $\boldsymbol{R}_{ij}$ is kept constant and only rotation is possible, the particle j will have an elongation ξ that depends only on its rotation between time t and the predictor step:

$$\xi_j^{(\mathrm{rot})}(t+\Delta t) = \xi_j^{(\mathrm{rot})}(t) + (\theta_j^p(t+\Delta t) - \theta_j^p(t))a_j, \tag{15}$$

where θ^p and $\theta(t)$ are the rotation angles of particle j till the predictor step and time step t, respectively.

When both translation and rotation of particle j occur, then the elongation is the superposition of both contributions, yielding $\xi_j = \xi_j^{(\mathrm{tr})} + \xi_j^{(\mathrm{rot})}$. Thus, using the expressions in Eqs. (14) and (15) one avoids the truncation error, typically of the order of $(\Delta t)^2$, inherent to the Cundall spring model (see Eqs. 6 and 7).

Figure 9 shows the relaxation time t_R as a function of the time integration step for the three situations above, namely when only rotation is considered, when only translation is considered and when both rotation and translation are allowed. As we see for all these cases, the relaxation time is independent on the time integration step. This is due to the fact that all quantities in the expression for ξ above are computed at the predictor step which has an error of the order of $(\Delta t)^6$, i.e., the error $(\Delta t)^2$ introduced in Eq. (7) is now eliminated. Therefore, with the expressions in Eqs. (14) and (15) one can use time integration steps significantly larger than with the original Cundall spring.

When considering discs, one does not take into account the shape of the particles. Next, we consider the more realistic situation of irregular polygonal-shaped particles. Motion of rigid particles with polygonal shape is more complicated than that of simple discs, since the contact point no longer lies on the vector connecting the centers of mass. Further, for polygons, one must also be careful when decomposing the dynamics of each particle into translation and rotation around its center of mass. This implies recalculating each time the position of the center of mass (only from translation) and the relative position of the vertices (only from rotation).

Therefore, for the translational contribution $\xi^{(\mathrm{tr})}$ in Eq. (14), we compute the overlap area between the two particles at t and at the predictor step. The overlap area is in general a polygon with a geometrical center that can be computed also at time t and the subsequent predictor step, yielding $\boldsymbol{r}_c(t)$ and $\boldsymbol{r}_c^p$, respectively. The increment for the translational contribution will be just the tangential projection $(\boldsymbol{r}_c(t) - \boldsymbol{r}_c^p) \times \hat{t}^c$. Similarly, the contribution from the (polygonal) particle rotation is computed by determining branch vectors, $\boldsymbol{r}_b(t)$ and $\boldsymbol{r}_b^p$, defined as the vectors joining the center of the particle and the center of the overlap area at time step t and the predictor step, respectively. Computing the branch vector at t and at the predictor step, one derives the angle defined by them, namely $\theta = \arccos\left(\boldsymbol{r}_b^p \times \boldsymbol{r}_b(t)/(r_b^p r_b(t))\right)$, where r_b^p and $r_b(t)$ is the norm of the corresponding branch vectors and the average value $(r_b^p - r_b(t))/2$, yielding an increment in Eq. (15) given by $\theta(r_b^p - r_b(t))/2$.

Figure 10 compares how the relaxation time varies with the normalized time step when the original Cundall approach is used (squares) and when our improved approach is introduced (circles). Clearly, the dependence

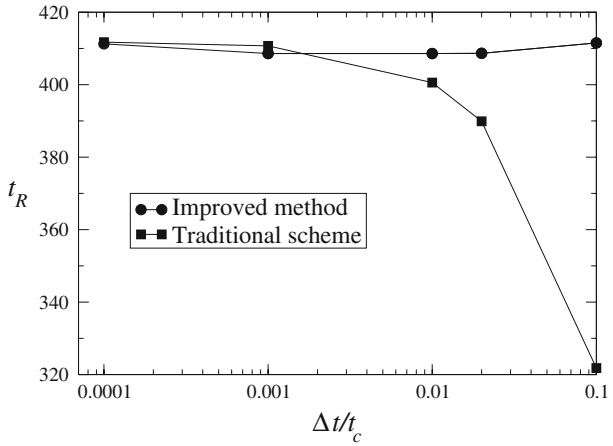

Fig. 10 Stress control test between two polygonal particles, as illustrated in Fig. 1. Comparison of the relaxation time t_R (in units of t_c) when using the standard integration scheme (*squares*) and the proposed improved scheme (*circles*). Here, rotation is neglected

on the time integration step observed for the usual integration scheme disappears when our improved approach is introduced. Therefore, all the conclusions taken above for discs remain valid for polygons.

5 Discussion and conclusions

In this paper we introduced a technique to improve the accuracy of the Gear's numerical scheme used to compute the evolution of granular systems.

To that end, we have first shown that the range of admissible time integration steps has an upper limit significantly smaller than typically used. The accuracy of the numerical scheme not only depends on the associated error when computing the particle positions (predictor–corrector scheme) with the Gear algorithm, widely used for granular media, but also on the accuracy when determining the frictional force, which is usually implemented by the Cundall spring. Since the Cundall spring is linear in the integration step, the overall accuracy of the numerical scheme cannot be higher than $(\Delta t)^2$. Therefore, when large time integration steps are required, e.g., in slow shearing, the numerical scheme does not give accurate results.

To overcome this problem we introduced an alternative approach for computing the frictional forces that suits not only the simple situation of discs but the more realistic situation of polygonal particles. Our approach takes into consideration the geometry and mechanical response of the particles and is particularly suited for situations where non-sliding contacts are relevant to the overall response. In general, for any other integration scheme, the substitution of the Cundall spring expression by the relations introduced in Eqs. (14) and (15), yields an error that is of the same order as the one associated with the predictor–corrector scheme. When using simplified models, e.g., samples of circular particles (discs), a third order model may suffice. However, for irregular particles the fifth order is usually needed for attaining convergence.

Inspired by the above results, some questions arise for forthcoming studies. The approach presented here should be considered when simulating shearing of system with many particles, as our initial example in Fig. 3. However, for these more complicated system where the breakage and generation of contacts occur, one must in parallel attend to carefully chose the contact point used for the calculations. Further, since the contact point is taken as the geometrical center of their overlap area, the branch vectors also vary during rotation, which is not taken into account in our present approach. These and other points will be addressed in the future.

Acknowledgments The authors thank Fernando Alonso-Marroquín for useful discussions. We thank for support by German-Israeli Foundation and by *Deutsche Forschungsgemeinschaft,* under the project HE 2732781. PGL thanks for support by *Deutsche Forschungsgemeinschaft*, under the project LI 1599/1-1. HJH thanks the Max Planck prize.

Appendix: The Gear's algorithm

To solve the equations of motion (1) we use the Gear's predictor–corrector scheme [9]. This scheme consist of three main stages, namely prediction, evaluation, and correction.

In the prediction stage the position, velocities, and higher-order time derivatives are updated by expansions of the corresponding Taylor series using the current values of these quantities [9,19]. For the position $\boldsymbol{r}$ of the center of mass these equations read

$$
\begin{aligned}
\boldsymbol{r}_{(t+\Delta t),p} &= \boldsymbol{r}_{(t)} + \dot{\boldsymbol{r}}_{(t)}\,\Delta t + \ddot{\boldsymbol{r}}_{(t)}\,\frac{\Delta t^2}{2!} + \boldsymbol{r}^{iii}_{(t)}\,\frac{\Delta t^3}{3!} + \boldsymbol{r}^{iv}_{(t)}\,\frac{\Delta t^4}{4!} + \boldsymbol{r}^{v}_{(t)}\,\frac{\Delta t^5}{5!},\\
\dot{\boldsymbol{r}}_{(t+\Delta t),p} &= \dot{\boldsymbol{r}}_{(t)} + \ddot{\boldsymbol{r}}_{(t)}\,\Delta t + \boldsymbol{r}^{iii}_{(t)}\,\frac{\Delta t^2}{2!} + \boldsymbol{r}^{iv}_{(t)}\,\frac{\Delta t^3}{3!} + \boldsymbol{r}^{v}_{(t)}\,\frac{\Delta t^4}{4!},\\
\ddot{\boldsymbol{r}}_{(t+\Delta t),p} &= \ddot{\boldsymbol{r}}_{(t)} + \boldsymbol{r}^{iii}_{(t)}\,\Delta t + \boldsymbol{r}^{iv}_{(t)}\,\frac{\Delta t^2}{2!} + \boldsymbol{r}^{v}_{(t)}\,\frac{\Delta t^3}{3!},\\
\boldsymbol{r}^{iii}_{(t+\Delta t),p} &= \boldsymbol{r}^{iii}_{(t)} + \boldsymbol{r}^{iv}_{(t)}\,\Delta t + \boldsymbol{r}^{v}_{(t)}\,\frac{\Delta t^2}{2!},\\
\boldsymbol{r}^{iv}_{(t+\Delta t),p} &= \boldsymbol{r}^{iv}_{(t)} + \boldsymbol{r}^{v}_{(t)}\,\Delta t,\\
\boldsymbol{r}^{v}_{(t+\Delta t),p} &= \boldsymbol{r}^{v}_{(t)}.
\end{aligned}
$$

From the equations above, one extracts a predicted position $\boldsymbol{r}_{(t+\Delta t),p}$ and acceleration $\ddot{\boldsymbol{r}}_{(t+\Delta t),p}$ for the center of mass of a given particle and the predicted angular displacement $\boldsymbol{\theta}^p(t+\Delta t)$ and angular acceleration $\ddot{\boldsymbol{\theta}}^p(t+\Delta t)$ of that particle around its center of mass.

An important point to stress here is that, since $\dot{\boldsymbol{r}}$ is of the order of magnitude of the shear rate $\dot{\gamma}$, situations of low shear naturally lead to a very slow evolution of the system, which implies the choice of a significantly large integration step Δt to achieve reasonable computational times. Consequently, if the admissible integration steps are to small, one naturally appeals for further improvement in this standard algorithm, as discussed in Sect. 3.

During the evaluation stage, one uses the predicted coordinates to determine the contact force $\boldsymbol{F}^c_{t+\Delta t}$ at time $t+\Delta t$. Since the method is not exact, there is a difference between the acceleration $\ddot{\boldsymbol{r}}(t+\Delta t) = \boldsymbol{F}^c_{t+\Delta t}/m$ and the value obtained in the prediction stage, namely

$$
\Delta\ddot{\boldsymbol{r}} = \ddot{\boldsymbol{r}}(t+\Delta t) - \ddot{\boldsymbol{r}}^p(t+\Delta t). \tag{17}
$$

The difference in Eq. (17) is used in the corrector step to correct the predicted position and time derivatives. This correction is performed using proper weights α_i for each time derivative [9], as follows [19]

$$
\begin{aligned}
\boldsymbol{r}_{(t+\Delta t)} &= \boldsymbol{r}_{(t+\Delta t),p} + \alpha_0 \frac{\ddot{\boldsymbol{r}}\Delta t^2}{2!},\\
\dot{\boldsymbol{r}}_{(t+\Delta t)}\,\Delta t &= \dot{\boldsymbol{r}}_{(t+\Delta t),p}\,\Delta t + \alpha_1\,\frac{\ddot{\boldsymbol{r}}\Delta t^2}{2!},\\
\ddot{\boldsymbol{r}}_{(t+\Delta t)}\,\frac{\Delta t^2}{2!} &= \ddot{\boldsymbol{r}}_{(t+\Delta t),p}\,\frac{\Delta t^2}{2!} + \alpha_2\,\frac{\ddot{\boldsymbol{r}}\Delta t^2}{2!},\\
\boldsymbol{r}^{iii}_{(t+\Delta t)}\,\frac{\Delta t^3}{3!} &= \boldsymbol{r}^{iii}_{(t+\Delta t),p}\,\frac{\Delta t^3}{3!} + \alpha_3\,\frac{\ddot{\boldsymbol{r}}\Delta t^2}{2!},\\
\boldsymbol{r}^{iv}_{(t+\Delta t)}\,\frac{\Delta t^4}{4!} &= \boldsymbol{r}^{iv}_{(t+\Delta t),p}\,\frac{\Delta t^4}{4!} + \alpha_4\,\frac{\ddot{\boldsymbol{r}}\Delta t^2}{2!},\\
\boldsymbol{r}^{v}_{(t+\Delta t)}\,\frac{\Delta t^5}{5!} &= \boldsymbol{r}^{v}_{(t+\Delta t),p}\,\frac{\Delta t^5}{5!} + \alpha_5\,\frac{\ddot{\boldsymbol{r}}\Delta t^2}{2!}.
\end{aligned}
$$

These weights depend upon the order of the algorithm and the differential equation being solved. In our simulations we integrate equations of the form $\ddot{\boldsymbol{r}} = f(\boldsymbol{r}, \dot{\boldsymbol{r}})$, and use a fifth order predictor–corrector algorithm [9]. The coefficients α_i for this situation are [9]: $\alpha_0 = 3/16$, $\alpha_1 = 251/360$, $\alpha_2 = 1$, $\alpha_3 = 11/18$, $\alpha_4 = 1/6$ and $\alpha_5 = 1/60$.

Finally, the corrected values are used for the next time step $t+\Delta t$, and the procedure starts again from these values to further integrate the system's evolution. The resulting numerical error for the fifth order integration scheme is proportional to $(\Delta t)^6$.

While the expansions above for $\boldsymbol{r}$ and corresponding time derivatives describe the dynamics of the center of mass of the particles, the same procedure is equally applied for the rotation angles θ_i around the center of mass as well as for their time derivatives.

References

1. Pöschel, T., Schwager, T.: Computational Granular Dynamics. Springer, Berlin (2005)
2. Ciamarra, M.P., Coniglio, A., Nicodemi, M.: Shear instabilities in granular mixtures. Phys. Rev. Lett. **94**, 188001 (2005)
3. da Cruz, F., Eman, S., Prochnow, M., Roux, J.N.: Rheophysics of dense granular materials: discrete simulation of plane shear flows. Phys. Rev. E. **72**, 021309 (2005)
4. Cundall, P.A.: Numerical experiments on localization in frictional materials. Ingenieur-Archiv **59**, 148 (1989)
5. Thompson, P.A., Grest, G.S.: Lasting contacts in molecular dynamics simulations. Phys. Rev. Lett. **67**, 1751 (1991)
6. Peña, A.A., García-Rojo, R., Herrmann, H.J.: Influence of particle shape on sheared dense granular media. Granul. Matter **9**, 279–291 (2007)
7. Alonso-Marroquín, F., Vardoulakis, I., Herrmann, H.J., Weatherley, D., Mora, P.: Effect of rolling on dissipation in fault gouges. Phys. Rev. E **74**, 031306 (2006)
8. Mora, P., Place, D.: The weakness of earthquake faults. Geophys. Res. Lett. **26**, 123 (1999)
9. Allen, M.P., Tildesley, D.J.: Computer Simulation of Liquids. Oxford University Press, Oxford (2003)
10. McNamara, S., Garía-Rojo, R., Herrmann, H.J.: Microscopic origin of granular ratcheting. Phys. Rev. E. **77**, 031304 (2008)
11. Luding, S., Clément, E., Blumen, A., Rajchenbach, J., Duran, J.: Anomalous energy dissipation in molecular-dynamics simulations of grains: the detachment effect. Phys. Rev. E **50**, 4113 (1994)
12. Cundall, P.A., Strack, O.D.L.: A discrete numerical model for granular assemblies. Géotechnique **29**, 47–65 (1979)
13. Tillemans, H.J., Herrmann, H.J.: Simulating deformations of granular solids under shear. Physica A **217**, 261–288 (1995)
14. Foerster, S.F., Louge, M.Y., Chang, H., Allia, K.: Measurements of the collision properties of small spheres. Phys. Fluids **6**(3), 1108 (1994)
15. Luding, S.: Collisions and contacts between two particles. In: Herrmann, H.J., Hovi, J.-P., Luding, S. (eds.) Physics of Dry Granular Media, pp. 285 Kluwer, Dordrecht (1998)
16. Matuttis, H.-G.: Simulation of the pressure distribution under a two-dimensional heap of polygonal particles. Granul. Matter **1**, 83 (1998)
17. Alonso-Marroquín, F., Herrmann, H.J.: Ratcheting of granular materials. Phys. Rev. Lett. **92**, 054301 (2004)
18. Latham, S., Abe, S., Mora, P.: Parallel 3D simulation of a fault gouge. In: García-Rojo, R., Herrmann, H.J., McNamara, S. (eds.) Powders and Grains 2005, p. 213. Balkema, Stuttgart (2005)
19. Rougier, E., Munjiza, A., John, N.W.M.: Numerical comparison of some explicit time integration schemes used in DEM, FEM/DEM and molecular dynamics. Int. J. Numer. Meth. Eng. **61**, 856 (2004)